Available online at www.CivileJournal.org

Civil Engineering Journal

(E-ISSN: 2476-3055; ISSN: 2676-6957)

Vol. 12, No. 02, February, 2026

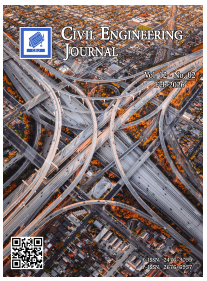

Scour Morphology Comparison Around Oblong Bridge Pier: Clear-Water and Live-Bed Flow Conditions

Achmad Rafi'ud Darajat [1, 2], Bambang A. Kironoto [1*], Istiarto [1]

[1] *Department of Civil and Environmental Engineering, Faculty of Engineering, Universitas Gadjah Mada, Yogyakarta, Indonesia.*

[2] *Department of Civil Engineering, Faculty of Engineering, Universitas Tidar, Magelang, Indonesia.*

Received 20 August 2025; Revised 22 December 2025; Accepted 04 January 2026; Published 01 February 2026

Abstract

Bridge pier scour is a significant contributor to structural instability in riverine infrastructure, particularly in sediment-laden tropical rivers. Streamlined shapes such as oblong piers generally produce smaller scour depths than bluff-body piers, offering potential safety advantages. However, the morphological evolution of scour under different sediment-transport regimes and its implications for structural stability remain insufficiently documented. This study experimentally compares clear-water (CW) and live-bed (LB) scour around an oblong pier, with emphasis on equilibrium depth, temporal development, three-dimensional morphology, velocity structure, and safety relevance. Flume tests were performed using a 5-cm × 10-cm oblong pier under steady subcritical flow (Q = 50 L/s, h = 10 cm, d_{50} = 2.21 mm, Fr < 1), with CW simulated by eliminating upstream sediment supply and LB by continuous sediment recirculation. Velocity measurements using an Acoustic Doppler Velocimeter (ADV) were conducted at equilibrium scour geometry to characterize flow structures. Results show CW scour reached a deeper equilibrium (z/D = 1.70), developed 36.4% faster (T^* = 666 min) than LB (z/D = 1.52, T^* = 909 min). CW formed a symmetric, steep-walled scour hole with 14.1% greater volume and 15.6% wider planform area, creating an immediate risk of vertical undermining. LB produced a shallower, more elongated scour with partial downstream backfilling, leading to gradual longitudinal undermining and slower foundation settlement. Velocity measurements revealed stronger vertical and lateral fluctuations under LB, explaining its more irregular scour morphology. Although the reduced scour depth confirms previous findings for streamlined piers, the elongated downstream scour and partial backfilling under LB provide new insights for countermeasure design. Among the tested predictors, Sheppard's Equation performed best with 8% (CW) and 3% (LB) deviations. These findings confirm that streamlined oblong piers reduce the maximum scour depth compared with circular shapes, but reveal contrasting mechanisms: CW promotes rapid, concentrated erosion, whereas LB induces slower, more widespread scour. The results emphasize that countermeasure design must explicitly account for the sediment-transport regime to ensure long-term foundation stability.

Keywords: Oblong Pier Scour; Clear-Water Scour; Live-Bed Scour; Scour Morphology; Velocity Measurements.

1. Introduction

1.1. Background and Engineering Relevance

Bridge pier scour is a significant cause of hydraulic-structure failure worldwide, especially in tropical river systems with high sediment loads and frequent flooding. Indonesia, the world's largest archipelagic country, provides a representative setting: its dynamic rivers demand resilient and adaptable bridge foundations to support socioeconomic connectivity and regional growth [1]. In these environments, bridge piers are crucial structural elements for medium-

* Corresponding author: kironoto@ugm.ac.id

https://doi.org/10.28991/CEJ-2026-012-02-023

and long-span crossings, yet they are highly vulnerable to local scour. It is estimated that nearly 47% of documented bridge failures are linked to scour and flood-related processes [2, 3].

Among various pier geometries, oblong-shaped piers including those with elliptical and oval cross-sections are increasingly used in modern bridge design because their streamlined shape reduces flow separation, turbulence, and vortex shedding compared to bluff-body shapes, such as cylindrical or rectangular piers [4, 5]. Laboratory studies have shown that oblong piers produce smaller, more compact horseshoe-vortex (HSV) cores than cylindrical piers under similar flow conditions [6, 7]. The rounded leading edge delays boundary-layer separation and weakens the downflow that initiates the HSV, as also noted by Graf & Yulistiyanto [4]. Despite these hydraulic advantages, oblong piers remain vulnerable to local scour during high flows and sediment-rich conditions, when scour depths can reach critical levels, endangering structural safety.

Local scour results from complex three-dimensional (3D) interactions between flow and sediment. An adverse pressure gradient at the upstream face causes a downflow that rolls into a U-shaped horseshoe-vortex [5, 8–10], while wake vortices develop downstream due to boundary-layer separation, creating turbulent eddies that entrain and transport sediment away from the scour hole [11, 12]. These vortex systems work together to lift and carry bed material downstream [8, 13, 14]. Scour occurs under two main sediment-transport regimes: clear-water (CW) scour, when no sediment is supplied from upstream, leading to continuous bed erosion and the formation of deeper, more stable scour holes; and live-bed (LB) scour, when upstream sediment supply is ongoing, establishing a dynamic balance between erosion and deposition and resulting in scour morphology that differs significantly from CW conditions [9, 10, 15]. These mechanisms are schematically illustrated in Figure 1.

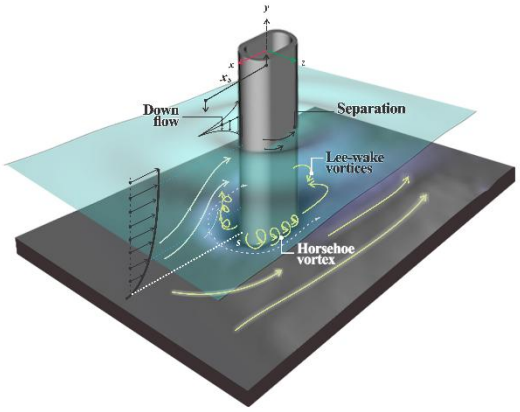

Figure 1. Conceptual flow pattern around an oblong pier, emphasizing vortex-induced scour mechanisms

1.2. State of the Art and Knowledge Gaps

Despite the rising use of oblong piers, systematic research on their scour behavior remains limited. Most empirical scour prediction formulas such as those proposed by Melville [16], the U.S. Federal Highway Administration (FHWA)'s HEC-18 guidelines [17], and Sheppard et al. [18] were designed for cylindrical or rectangular piers and may not accurately reflect the hydrodynamic and sediment-transport features of streamlined shapes [8, 19–21]. Recent laboratory studies, including those by Chavan et al. [7], Bento et al. [22], and Baduna Koçyiğit & Koçyiğit [23], have enhanced understanding of flow around oblong piers and showed the spatial variability of scour geometry under controlled flume conditions. Omara et al. [24] also studied how changing water levels affect scour development around cylindrical and oval piers.

However, most of these investigations have concentrated on CW conditions or transient water-level effects, leaving LB scour scenarios poorly understood. Furthermore, most previous experiments only report the maximum equilibrium scour depth, offering limited insight into the 3D shape and how scour holes evolve over time both are essential for validating predictive models [25]. Experimental validation of near-bed velocity fields and bed shear stresses over realistic scour topography remains limited as well [22, 26]. As a result, no prior study has integrated high-resolution laser-based bed profiling with simultaneous three-dimensional flow measurements to observe the spatial and temporal development of scour around oblong piers in LB conditions. This lack of comprehensive laboratory data hampers the ability to accurately calibrate empirical formulas and impedes the development of reliable design guidelines for bridges in sediment-rich tropical rivers. Field measurements in actual river conditions, such as those conducted by Silvia [27] at the Krueng Ineng River, provide valuable documentation of scour magnitude in real settings. However, controlled laboratory experiments remain essential for isolating and understanding the fundamental flow-sediment-structure interactions under various sediment transport regimes.

1.3. Research Objectives and Contributions

This study investigates how CW and LB sediment conditions influence the development and three-dimensional shape of scour around oblong bridge piers. Specifically, it aims to: (i) compare scour progression and 3D geometry under CW and LB conditions; (ii) analyze velocity fields and near-bed shear stresses using high-resolution measurement techniques; and (iii) evaluate the applicability of existing empirical scour prediction models for streamlined pier designs.

Experiments were performed in a recirculating sediment flume designed to maintain LB equilibrium through consistent sediment feed and feedback control, enabling accurate replication of various scour regimes. Temporal and three-dimensional scour-hole development was recorded using laser displacement sensors, while Acoustic Doppler Velocimetry (ADV) provided detailed three-dimensional velocity profiles upstream and downstream of the pier over the changing bed. This integrated approach offers a high-resolution, unique dataset that supports the calibration and validation of empirical scour prediction models and enhances understanding of flow–sediment–structure interactions around streamlined pier shapes. The findings are expected to improve scour-risk assessments, early-warning systems, and the development of effective countermeasures, especially for bridges constructed in sediment-rich tropical rivers.

The rest of this work is organized as follows. Section 2 presents the theoretical background, explaining key hydraulic and sediment-transport parameters and their important dimensionless relationships. It also covers the temporal development of scour, near-bed velocity distribution, and related bed shear stress. Section 3 details the experimental methodology, including the flume setup, sediment properties, flow conditions, and measurement techniques. Section 4 displays the results, including scour progression, three-dimensional scour morphology, velocity profiles, and an assessment of empirical scour-prediction models. Finally, Section 5 summarizes the main conclusions and emphasizes the engineering importance of the findings.

2. Theoretical Background

This section lays out the theoretical foundation for analyzing CW and LB scour around oblong bridge piers. It combines key concepts from open-channel hydraulics, sediment-transport mechanics, and vortex-driven scour to guide experimental design and result interpretation. Unlike physical modeling studies focused on prototype scaling, this research is process-oriented, employing dimensionless relationships as a conceptual framework to identify the main parameters and facilitate comparison with empirical scour prediction models. The section introduces the key hydraulic and sediment-transport parameters, and their general non-dimensional relationships, explains the timing of scour development, and describes the velocity distribution as a physical reference, before connecting these ideas to the empirical models discussed in Section 3.

2.1. Governing Hydraulic and Sediment-Transport Parameters

The theoretical understanding of scour around streamlined piers can be formalized using dimensional analysis. According to Buckingham's π-theorem, the equilibrium scour depth z can be expressed as a function of key non-dimensional groups:

$$\frac{z}{D} = f\left(Fr, Re, \frac{d_{50}}{D}, \left(\frac{h}{D}\right), \sigma_g, k_{sh}, \frac{\tau_*}{\tau_{*cr}}, \frac{t}{T^*}\right) 1 \quad (1)$$

Here z represents the maximum equilibrium scour depth, D is the characteristic pier width (minor axis for oblong), $Fr = U/\sqrt{(g\ h)}$ is the Froude number characterizing flow intensity, and $\mathrm{Re} = UD\ /\ v$ is the Reynolds number for turbulence effects, d_{50}/D represents relative sediment size, and h/D denotes relative flow depth, $\sigma_g = \sqrt{(d_{84}/d_{16})}$ is the geometric standard deviation of sediment gradation, τ_* is the Shields parameter, and τ_{*c} is its threshold, k_{sh} accounts for pier geometry effects, where the mobility parameter (τ_*/τ_{*cr}) distinguishes between CW $(\tau_*/\tau_{*cr} \leq 1.0)$ and LB $(\tau_*/\tau_{*cr} > 1.0)$ conditions, and t/T^* indicates temporal development relative to characteristic time. This theoretical framework provides the foundation for understanding how streamlined pier geometries interact with different sediment-transport regimes and guides the experimental design employed in this study.

In this study, the adopted compact relationship is not intended as a new predictive Equation but rather as a conceptual map of the hydraulic and sediment-transport parameters that influence local scour around oblong bridge piers. By organizing these governing non-dimensional variables, it provides a rigorous analytical framework for selecting experimental conditions-such as approach velocity, sediment size, and pier geometry structuring the analysis of scour behavior and examining the three-dimensional development of scour morphology over time. This framework also supports systematic comparison with well-established empirical formulas.

Collectively, the identified parameters capture the key physical processes that cause local scour-namely, HSV downflow, wake-vortex sediment entrainment, and the interaction of approach flow turbulence with a movable bed. By explicitly linking these mechanisms to measurable non-dimensional groups, the adopted compact relationship provides the conceptual and methodological foundation for this research, ensuring that the experimental design and subsequent data interpretation remain physically consistent and aligned with standard hydraulic engineering practices.

2.2. Time Characteristics of Scour Development

The temporal evolution of scour depth, $z(t)$, is described using the exponential growth model by Oliveto & Hager [28]:

$$z(t) = z_{eq}\left[1 - exp\left(-\frac{t}{T*}\right)\right] \quad (2)$$

where T^* is the characteristic time of the scour process, indicating how rapidly the scour approaches equilibrium. A smaller T^* signifies a faster progression toward z_{eq}. According to Melville & Coleman [19], T^* is defined as the characteristic time at which the scour depth reaches approximately 63.2% of its equilibrium value. This formulation describes three distinct stages of scour development: an initial rapid phase dominated by intense HSV downflow and wake-vortex sediment transport; a transitional stage where the scour rate declines as sediment entrainment and deposition move toward equilibrium; and an asymptotic stage during which the scour depth gradually approaches equilibrium. T^* provides a physical measure of scour kinetics. It is used to interpret time-series scour data and to highlight differences in temporal dynamics between CW and LB regimes in the laboratory experiments.

2.3. Velocity Distribution and Bed Shear Stress

Near-bed turbulence and the forces responsible for sediment mobilization are described by the logarithmic velocity law for rough-bed open-channel flow [29].

$$\frac{u(z)}{u_*} = \frac{1}{\kappa} ln\left(\frac{z}{k_s}\right) + Br \quad (3)$$

where $u(z)$ is the mean streamwise velocity at elevation z, u_* is the friction velocity, and κ is the von Kármán constant (≈ 0.40). The roughness length, which is related to the sediment size, is associated with the effective Nikuradse roughness, $k_s \approx d_{50}$, and Br is a constant that depends on the roughness regime. In practice, u_* and k_s are obtained from a linear fit of u/u_* versus ln(z) within the constant-stress layer, typically up to ~ $0.2h$, where h is the flow depth. This formulation provides the physical basis for understanding how near-bed turbulence and bed shear stress influence sediment entrainment and the formation of scour holes. It also serves as a theoretical reference for interpreting flow–sediment–structure interactions around an oblong pier, even though detailed turbulence measurements and explicit computation of shear velocity (u_*) are beyond the scope of this paper.

3. Methodology and Experimental Setup

The detailed experimental methodology used in this study is illustrated in the flowchart in Figure 2, which presents a systematic approach for examining equilibrium scour characteristics and flow-velocity distribution around oblong bridge piers. The research involved two main phases: first, scour-equilibrium experiments were conducted under clear-water (CW) and live-bed (LB) conditions to establish baseline morphological patterns; second, flow-velocity measurements were taken using Acoustic Doppler Velocimetry (ADV) to analyze the governing flow mechanisms.

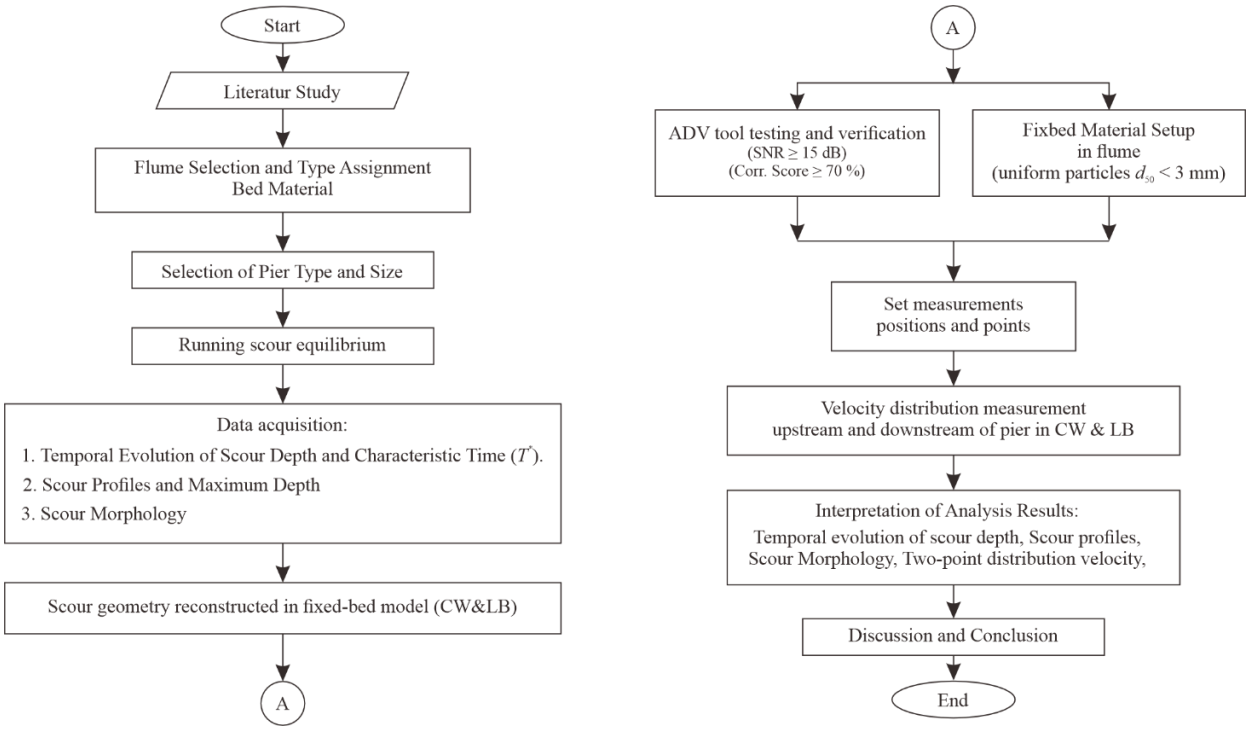

Figure 2. Experimental workflow for scour investigation around oblong bridge piers

The experimental program started with selecting a recirculating flume and carefully designing the oblong pier shape. The pier's form and size were chosen to resemble a streamlined bridge pier, reducing wall effects while allowing fully developed turbulent flow around the structure. Before each scour test, extensive hydraulic calibration was performed to establish stable baseline conditions, ensuring the approach flow was fully developed and sediment transport had reached equilibrium. These preparatory steps ensured that the interaction between the incoming flow and the pier shape was consistent and could be reliably repeated at the beginning of each test.

Scour tests were then performed with the chosen pier design and monitored until reaching the equilibrium scour depth. During this phase, high-resolution measurements captured the time-dependent development of scour and the three-dimensional shape of the scour hole formed around the oblong pier. To obtain accurate velocity-distribution measurements without interference from sediment movement, the final equilibrium scour topography was later reconstructed using a fixed-bed setup. This reconstruction preserved the exact pier–bed geometry at equilibrium, allowing for a precise analysis of the complex three-dimensional flow patterns influenced by the pier shape.

Throughout the experimental program, an iterative quality control framework was employed. Measurement parameters were adjusted as necessary to maintain consistent target Reynolds numbers and sediment-mobility conditions, ensuring that all runs remained physically valid and met the required data-quality standards. The reliability of ADV velocity measurements was further verified using signal-to-noise ratio (SNR) thresholds of 15 dB or higher and correlation-level criteria of 70% or higher. This step-by-step, quality-assured approach provides a solid foundation for analyzing the interactions among flow dynamics, sediment transport, and scour morphology around oblong bridge piers.

3.1. Flume Configuration and Hydraulic System

The laboratory experiments were conducted in a 10-m-long sediment recirculating flume located at the Hydraulics Laboratory, Department of Civil and Environmental Engineering, Universitas Gadjah Mada, Yogyakarta, Indonesia. The flume has a rectangular cross-section of 0.60-m in width and 0.50-m in depth, and is equipped with essential hydraulic components, including a tailgate, sediment trap, circulation pump, sump tanks, head box, and flow control instruments.

A general overview of the experimental facility and its main components is shown in Figure 3, while a more detailed schematic of the internal configuration, sediment routing, and instrumentation setup is provided in Figure 4. This figure offers a comprehensive view of the flume layout, enabling consistent implementation and comparison of both sediment-fed (LB) and sediment-starved (CW) flow conditions.

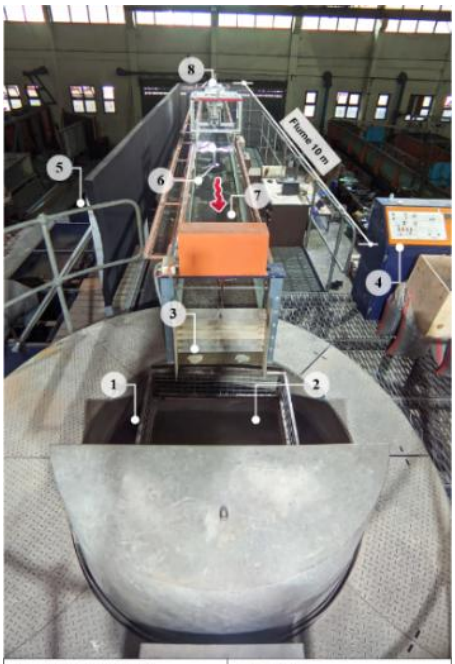

1 = Tank sirkulation	5 = Sump
2 = Box sedimen trap	6 = Oblong Pier
3 = Tail gate	7 = Bed Material d_{50}
4 = Navigation instrument	8 = Head box (Inlet)

Figure 3. Experimental flume setup and key components used in the scour tests

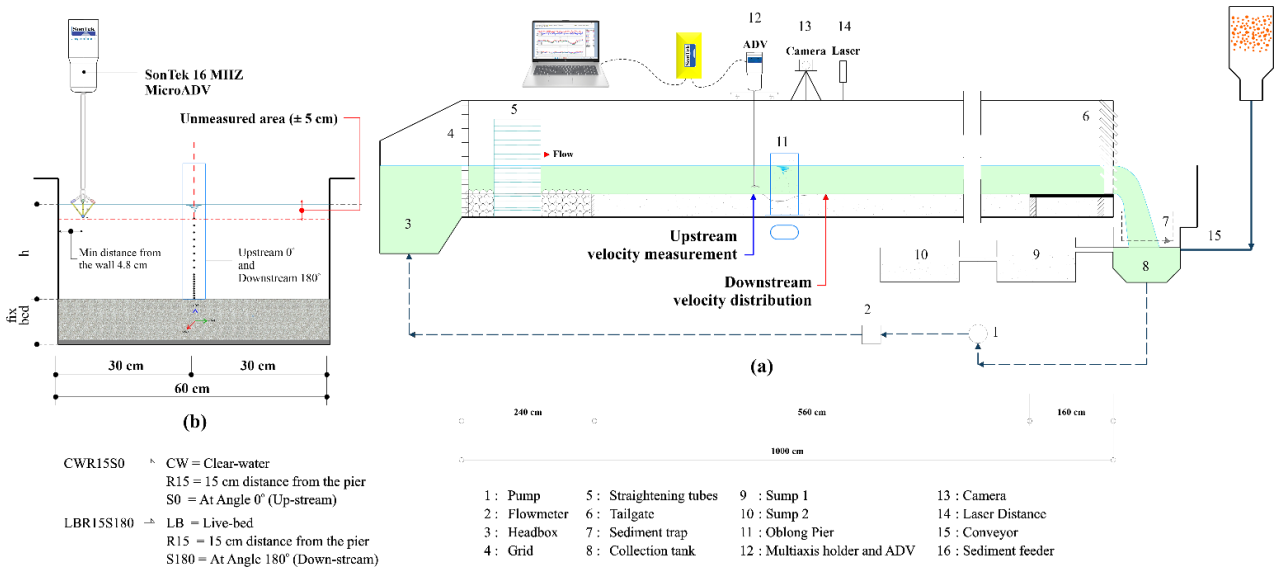

Figure 4. (a) Schematic of the experimental setup; (b) Vertical measurement positions

The system operates with a closed-circuit setup, supported by a secondary circulation pump. This design allows flexible operation in CW and LB conditions. During LB scour tests, sediment carried by the flow is continuously recirculated through a looped piping system that bypasses the sump tanks, preventing unwanted sediment buildup. For CW scour experiments, the upstream sediment supply is intentionally cut off, and eroded materials are collected in a downstream sediment trap to simulate conditions without upstream sediment-transport. Flow is directed through a network of seven valves, two manually operated and five electrically controlled, allowing precise regulation of water discharge and sediment movement. Before each LB test, preliminary adjustments are made to establish equilibrium sediment-transport conditions, ensuring the sediment feeding rate matches the transport capacity at the target discharge. The initial adjustment involves carefully controlling both the flow discharge and the sediment feeding rate until a steady-state transport condition is achieved. Sediment-transport equilibrium is confirmed through this initial adjustment, where the sediment-feeding rate is fine-tuned until the difference between inlet and outlet sediment concentrations is less than 5%, with stable conditions maintained over 180 min of continuous operation.

As shown in Figure 4, the experimental flume is divided into three sections. The upstream section, 2.4-m long, is filled with coarse gravel to dissipate turbulence caused by the inflow from the closed-circuit system, ensuring a uniform velocity profile and stable flow conditions as water enters the main test section.

3.2. Sediment and Flow Conditions

In the CW experiments, the flume runs without any upstream sediment input. Sediment eroded around the pier is collected in a downstream sediment trap, simulating a non-compensated scour environment. In contrast, the LB experiments use a closed-loop sediment recirculation system, comprising a circulation pump and a sediment mixing tank, to supply sediment throughout the test continuously. This setup mimics a dynamic equilibrium where erosion and deposition occur simultaneously and continuously, similar to natural sediment-laden river systems.

The key difference between CW and LB conditions can be explained using the Shields parameter (τ_*), which represents the ratio of applied bed shear stress to the critical shear stress for sediment motion. CW scour occurs when $\tau_* < \tau_{*c}$, meaning that the applied shear stress is insufficient to mobilize the bed and no sediment is supplied from the upstream inflow, whereas LB scour occurs when $\tau_* > \tau_{*c}$, allowing continuous sediment transport from the upstream inflow. This threshold determines whether the flow can entrain sediment particles, thus directly controlling the initiation and development of scour around the pier.

This setup meets the recommended hydraulic design criterion of a flume width-to-pier width ratio (b/D) $\approx$ 12, exceeding the usual minimum of 8 to reduce wall effects and ensure accurate flow conditions. The experiment used a steady discharge of Q = 50 L/s and a flow depth of h = 10 cm, resulting in fully turbulent and subcritical flow, as indicated by a Reynolds number (Re) of approximately 43,000 and a Froude number (Fr) less than 1. Although this was not intended as a prototype-scale experiment, the chosen pier width of 5 cm corresponds to typical field oblong piers measuring approximately 1.0 to 1.5-m, suggesting an approximate geometric scale of 1:20–30, and confirming stable sediment movement under the tested conditions.

The sand used as the bed material was oven-dried and mechanically sieved to ensure a consistent grain-size distribution. It is nearly uniform, with a median grain diameter (d_{50}) of 2.21 mm and a coefficient of uniformity

($C_u = d_{84}/d_{16}$) of approximately 2.3, placing it at the lower end of the moderately sorted category and approaching well-sorted conditions according to the classifications of Folk & Ward [30], Buffington & Montgomery [31], and Blott & Pye [32]. This grain-size consistency benefits laboratory scour studies by reducing size segregation during sediment transport. Hydraulically, the sand behaves as a rough bed material, as indicated by a particle Reynolds number (Re_*) ≥ 70. The oblong pier used in the experiments had a width (D) of 5 cm—less than 10% of the total flume width (B = 60 cm)—thereby limiting wall-interference effects [4, 5]. To comprehensively characterize the sediment used in this study, a grain-size distribution analysis was performed in accordance with ASTM D6913. A representative 2-kg sample was mechanically sieved through standard mesh sizes ranging from 4.75 to 0.075 mm. The resulting grain-size distribution curve (Figure 5 and Table 1) shows the cumulative percentage of sediment finer than each sieve size. The analysis indicates that the sediment is nearly uniform, with a median grain diameter (d_{50}) of 2.21 mm and a coefficient of uniformity ($C_u = d_{84}/d_{16}$) of about 2.3. The geometric standard deviation ($\sigma_g = (d_{84}/d_{16})^{0.5}$ = 1.41) further confirms a moderately well-sorted material.

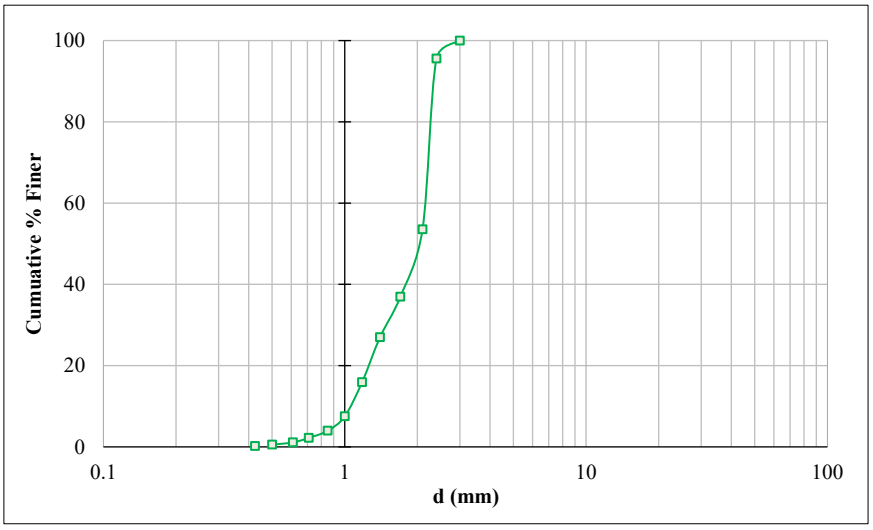

Figure 5. Grain-size distribution curve

Table 1. Sediment properties and classification parameters

Parameter	Value	Standard
Median grain size (d_{50})	2.21 mm	ASTM D854
d_{16}	1.56 mm	ASTM D6913
d_{84}	3.12 mm	ASTM D6913
Coefficient of uniformity (C_u)	2.33	Calculated
Geometric standard deviation (σ_g)	1.41	Calculated
Specific gravity (G_s)	2.65	ASTM D854

Photographic comparisons of these flow regimes are shown in Figure 6. The left image depicts a CW condition characterized by a visibly transparent water column, indicating the absence of upstream sediment supply. In contrast, the right image shows a LB condition with high suspended sediment concentration, reflecting active sediment-transport processes. By maintaining consistent sediment properties and hydraulic discharge across both scenarios, the study ensured that the observed differences in scour morphology were mainly caused by the sediment-transport regime (CW vs. LB), rather than fluctuations in sediment characteristics.

Figure 6. Experimental flow regimes: clear-water condition (left) and live-bed condition (right)

3.3. Bed Topography Measurement

To measure detailed changes in bed elevation, a high-precision laser displacement sensor was used (Figure 7). The sensor (Leica Disto X310) was mounted on a manually operated traverse system spanning the entire width of the flume, allowing systematic scanning of the bed surface in both the longitudinal (x) and transverse (y) directions. Measurements were taken at 2-mm intervals, with the sensor emitting a vertically aligned laser beam to determine the distance to the bed.

Figure 7. Laser displacement sensor for bed-topography measurement

This setup produced high-resolution, point-by-point elevation data across the entire test section, which was compiled into three-dimensional (X, Y, Z) point cloud data. The collected dataset was then processed to create a high-fidelity Digital Elevation Model (DEM), as the basis for quantitative analysis of scour-induced bed changes. This systematic scanning approach ensured data accuracy and consistency throughout the domain. The resulting DEM provided a reliable foundation for morphological analysis, especially around the pier where detailed bed deformation was expected. The high-resolution dataset enabled a thorough evaluation of spatial scour patterns and supported the interpretation of flow structure and sediment interaction dynamics.

3.4. Velocity Field Measurement

To investigate the three-dimensional flow characteristics around the oblong pier, velocity measurements were conducted using a Sontek 16-MHz MicroADV (Acoustic Doppler Velocimeter) probe with a 99% accuracy rate. These measurements were conducted on a reconstructed fixed-bed replicating the equilibrium scour geometry to avoid transient fluctuations from evolving bedforms. This approach eliminated the unsteady feedback between sediment entrainment and bed changes, ensuring stable and reproducible velocity profiles. Thus, the hydraulic influence of the final scour topography could be isolated, providing clearer insight into flow–structure interactions [33].

Under steady and uniform flow conditions, three-dimensional velocity components (u, v, and w) were measured at a sampling frequency of 50 Hz for 120 seconds, resulting in 6,000 instantaneous data points at each location. The ADV probe (Figure 4b) was positioned 1.5D upstream (0°) and downstream (180°) of the pier centerline, targeting regions of maximum HSV activity and wake formation. Vertical velocity profiles were recorded at 2-mm intervals from the bed (z/H = 0.02) up to near the free surface ($z/H \approx 0.6$); the upper water column could not be captured due to instrument limitations. The collected velocity data were processed using standard filtering techniques to remove noise and enhance data quality, with mean velocity values calculated from the time-averaged measurements. Data quality was evaluated based on signal-to-noise ratio (SNR) thresholds (>15 dB) and correlation levels (>70%) to confirm measurement validity and reliability. Besides the standard criteria of SNR and correlation level, additional filtering was performed in the SonTek ADV software using a conservative low-pass filter with a 15-Hz cutoff to reduce high-frequency noise, along with despiking via the Phase-Space Threshold (PST) method with a ±4σ threshold to eliminate outliers from velocity signals. These two extra filtering techniques have been proven to preserve turbulence spectral characteristics (-5/3 slope) and produce high-quality data with less than 1% data adjustment, ensuring that the turbulence parameters derived are statistically robust and physically meaningful [34]. These comprehensive velocity measurements provide quantitative insights into flow-structure interactions responsible for sediment transport and scour development around streamlined bridge piers.

4. Results and Discussions

4.1. Temporal Evolution of Scour Depth and Characteristic Time (T^*)

Figure 8 illustrates the temporal evolution of maximum scour depth along various azimuthal planes around the oblong pier. The experiment was conducted over a period of 48-h, which is consistent with the range of equilibrium times reported in the literature. Although some studies reported reaching equilibrium quickly, for instance, Chavan et

al. [7] reported equilibrium after 12-h, others required longer periods, such as Ettema et al. [8] and Sheppard et al. [18] who reached equilibrium after 24-h, Melville & Chiew [15] and Raudkivi & Ettema [35] who reported equilibrium at 48-h. This variation in equilibrium time depends on experimental conditions, including pier geometry, sediment characteristics, flow intensity, and transport regime. Based on this literature review, indicating equilibrium times ranging from 12 to 48 hours, the present study adopted a 48-h observation period to ensure complete scour development under both CW and LB conditions.

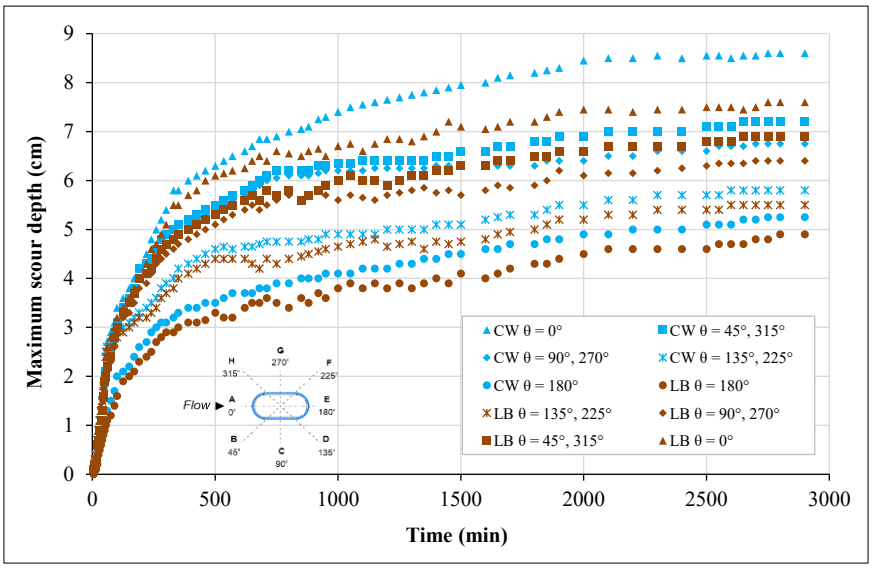

Figure 8. Time development of maximum scour depth in azimuthal half-planes

Under CW conditions, scour progressed more rapidly and reached a maximum depth of 8.5 cm at θ = 0°, corresponding to the upstream face of the pier, where flow separation and downflow concentrate erosional forces. This aligns with previous findings [5, 7, 8, 15, 18, 25, 28, 36], which identified the upstream face as the zone of highest erosional activity. The resulting scour profile exhibited clear azimuthal asymmetry, with depth gradually decreasing toward downstream directions (θ = 180°), creating a stable, deposition-free bed as noted by Farooq & Ghumman [25]. In contrast, LB scour developed more slowly and reached a shallower maximum depth of 7.6 cm at θ = 0°. The continuous upstream supply of sediment lessened scour severity by partially refilling the scour hole during erosion. This resulted in a smoother azimuthal distribution with smaller depth differences between angular positions (see also Figure 10 in Section 3.2). This supports the idea that sediment transport produces a leveling effect across the scour region, aligning with findings from [36–39] that described LB scour as a dynamic balance of erosion and deposition.

Across the off-axis azimuths (θ = 45°, 90°, 135°, 225°, 270°, and 315°), CW consistently produced greater scour depths than LB. At θ = 45° and 315° (the oblique sides), CW formed the second-deepest pockets after θ = 0°, whereas LB showed attenuated peaks from partial infilling. At the lateral positions (θ = 90° and 270°), CW depths were modest, while LB depths were slightly shallower and more evenly distributed. In the downstream oblique sectors (θ = 135° and 225°), CW exhibited moderate scour interspersed with localized deposition, whereas LB was largely governed by partial infilling, yielding the smallest depths and the flattest azimuthal gradients. Overall, LB compressed the azimuthal depth ranges relative to CW, producing a more uniform planform around the pier.

These differences in both spatial and temporal scour characteristics emphasize the contrasting mechanisms under CW and LB regimes. In CW, unobstructed sediment removal leads to rapid scour development, while in LB, the interaction between sediment inflow and hydraulic conditions results in a more uniform and delayed scour process. Notably, 90% of maximum scour under CW was achieved within roughly 1000 min, whereas LB conditions took much longer to reach equilibrium. This delay highlights the complex balance of erosion and deposition inherent in sediment-transport-dominated environments.

To estimate the characteristic time (T^*) of scour development, two analytical methods were used on the same experimental time-series data. The first method is threshold-based, defining T^* as the time when the scour depth reaches 63.2% of its equilibrium value (z_{eq}), as proposed by Melville & Chiew [15]. This criterion is derived from the analytical solution of the exponential growth Equation and does not require curve fitting. The second is an exponential-regression method, where the time-series data are fitted to $z(t) = z_{eq}[1 - \exp(-t/T^*)]$—usually using a semilogarithmic transformation—to find T^* from the best-fit curve. Both methods are based on the same theory but differ in execution: the threshold-based approach uses a single depth criterion, while the regression method describes the entire temporal development of scour. Comparing T^* values under CW and LB conditions offers insights into the time scales of scour processes and assesses the effectiveness of exponential modeling.

Based on the 63.2% criterion of the equilibrium scour depth (z_{eq}), the threshold depths corresponding to the characteristic time (T^*) were approximately 0.054 m for CW and 0.048 m for LB. Time-series measurements of scour depth were analyzed to identify when these thresholds were reached. As shown in Figure 7, the thresholds occurred at approximately 500–550 min for CW and 600–650 min for LB, with the earliest occurrence at $\theta = 0°$. At $\theta = 45°$ and 90°, the thresholds were reached slightly later, reflecting the slower development of scour away from the upstream face. These times are therefore considered estimates of T^* under each condition.

Beyond 1500 min, the scour–time curves reach a clear plateau, indicating a significant slowdown in scour growth. This pattern suggests the system is approaching a steady or near-equilibrium state. For practical Melville and Chiew [15] purposes, the time to reach 95% of the equilibrium scour depth (z_{eq}), a commonly adopted criterion for defining practical equilibrium, can be estimated using the empirical relation $t_{eq} \approx 3T^*$. Although the $3T^*$ relationship was originally developed for circular piers, its application to oblong piers is justified by the universal nature of the exponential scour development model and the similar fundamental mechanisms governing temporal scour evolution. With a total duration of 48-h (about 2880 min), the current experiments significantly exceed this threshold, providing the necessary duration to observe equilibrium scour conditions for both CW and LB scenarios. Although greater fluctuations were observed under LB conditions due to the dynamic interplay between sediment erosion and deposition, the convergence of scour depth after 1500 min indicates that a dynamic equilibrium was reached. These findings confirm that the measured z_{eq} values accurately reflect the equilibrium state, providing a solid empirical basis for further modeling and regression analysis.

The faster scour development under CW conditions (T^*= 666 min vs 909 min) reflects fundamental differences in erosional processes. CW conditions create an erosion-only environment where the HSV continuously removes bed material without interference. This unimpeded removal allows rapid deepening as the HSV maintains high intensity throughout development. LB conditions involve dynamic competition between erosion and partial backfilling. Continuous sediment supply creates a buffering effect where transported particles partially fill the developing scour hole, reducing the effective erosion rate. For the second method, in Figure 9, the time-series data were fitted to the classical exponential growth model using a semilogarithmic transformation following Equation 2. The fitted curves and the corresponding regression-based T^* values are shown in Figure 9, along with a discussion of the model's accuracy and its implications for assessing equilibrium conditions. Using the experimental data, linear regression was performed on the transformed exponential Equation, applied only to the data segment that displayed a clear linear trend in the semilog plot. This method finds widespread application in scour evolution studies, as evidenced by the work of Melville & Chiew [15] and Sheppard & Miller [38], particularly when the scour process exhibits an ideal exponential growth pattern during the early to middle stages. Scour development often diverges from the ideal model in the initial phase due to the establishment of flow or adjustments to boundary conditions, and again near equilibrium when the system begins to stabilize. Consequently, researchers like Breusers [40] and Cardoso & Bettess [41] have recommended excluding data points from the regression that show significant deviations from linearity, typically at the beginning and final saturation stages, to ensure accurate T^* estimation.

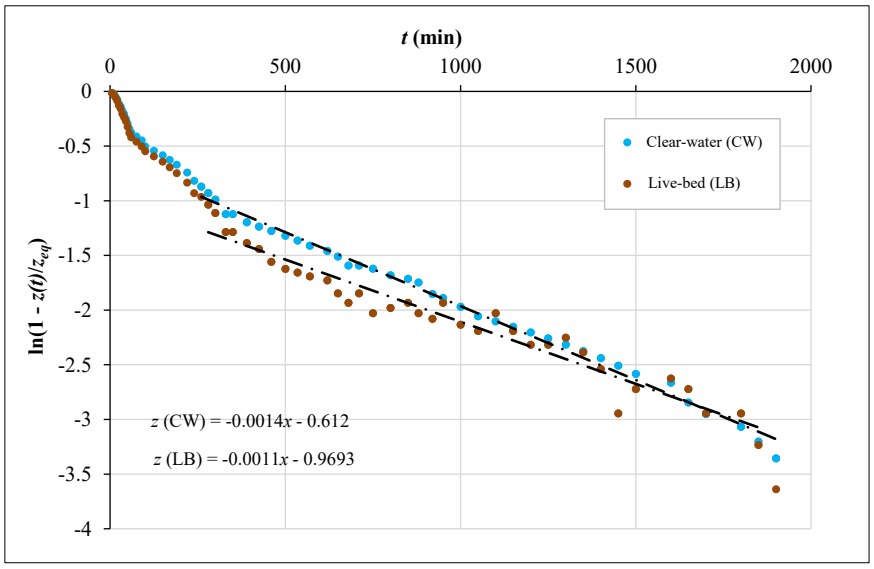

Figure 9. Time relationship to equilibrium scour

Although this selective fitting provides a representative characteristic time for the exponential growth phase, it may differ from values directly estimated from raw time–depth curves, as it only reflects the idealized portion of scour development. From Figure 8, the slope of the regression line for the CW condition was −0.0014, resulting in a

characteristic time (T^*) of 666 min. For the LB condition, the slope was −0.0011, leading to T^* of 909 min. This indicates that the scour process under CW conditions reaches equilibrium approximately 1.27 times faster than under LB conditions.

Using the T^* values, the practical time needed to reach 95% of the equilibrium scour depth can be estimated with the empirical relation $t_{eq} \approx 3T^*$. Therefore, the time to reach equilibrium is approximately 1998 min for CW (*i.e.*, 3 × 666), which corresponds to 95% of z_{eq} = 8.5 cm, and 2727 min for LB (*i.e.*, 3 × 909), corresponding to 95% of z_{eq} = 7.6 cm. These figures support the experimental finding that CW scour develops more rapidly due to unobstructed bed erosion, whereas LB scour progresses more slowly due to dynamic sediment exchange.

Additionally, the initial scour rate, dz/dt, was 0.013 cm/min for CW and 0.008 cm/min for LB, indicating that the rate in CW was approximately 62.5% higher than that in LB. The initial scour rate reflects the steepness of the early part of the $z(t)$ curve and demonstrates how quickly scour begins. This further supports the idea that sediment supply significantly influences both the initial rate and the overall development of local scour under live-bed conditions. This quantitative analysis confirms the experimental observation that CW scour progresses more quickly than LB scour. A summary of the key parameters from this temporal analysis is presented in Table 2.

Table 2. Summary of quantitative temporal analysis

Parameter	CW	LB	Difference
Scour depth (z_{eq})	8.5 cm	7.6 cm	CW > 11.8%
Time characteristics (T^*)	666 min	909 min	LB > 36.4%
Initial scour rate (dz/dt)	0.013 cm/min	0.008 cm/min	CW > 54.3%

The temporal evolution patterns observed in this study align with the three-stage scour development framework identified by Ahmad et al. [42] for wide piers, which comprises initial formation, main erosion, and equilibrium. However, the findings also reveal distinct differences due to pier geometry and sediment-transport regimes. The 48-h experimental duration used here was longer than the 13–25 hours employed by Ahmad et al. [42] for wide circular and rectangular piers (D/d_{50} = 75–717). This longer duration reflects the added temporal complexity of LB conditions, where continuous scour and refill cycles require extended observation periods to accurately determine equilibrium. The characteristic times obtained for oblong piers (T^* = 666–909 min) fall within the range reported for various pier geometries. The 36.4% increase from CW to LB conditions demonstrates a sediment transport effect that is comparable in magnitude to the geometric effects documented by Ahmad et al. [42]. Although Ahmad et al. found that 50% of the equilibrium depth was reached within 0.7%–11% of the total equilibrium time for wide piers, this study's 63.2% depth characteristic time threshold criterion (T^*) occurred at approximately 23% and 31.6% of the total experimental time for clear-water and live-bed conditions, respectively. This suggests that streamlined oblong geometries develop scour differently over time compared to bluff-body wide piers. Overall, these findings indicate that although pier geometry influences the temporal evolution of scour-as shown in previous research sediment-transport regimes are an equally important factor. Incorporating both into predictive models is essential for comprehensive bridge foundation design in sediment-laden river environments.

4.2. Scour Profile and Maximum Depth

The equilibrium bed contours reveal clear differences in scour morphology around the pier between CW and LB conditions (Figures 10 and 11). Under CW conditions, the scour hole is deeper and has a smooth, elongated shape with steep upstream side slopes. The maximum depth reaches 0.085 m (z/D = 1.70), localized upstream due to intense flow impact, and is considered the equilibrium scour depth (z_{eq}), beyond which further scour is minimal. The morphological distinctions reflect the contrasting hydraulic regimes, with CW developing well-defined scour holes and LB showing more irregular contours due to sediment interactions. Erosion is focused along the upstream and downstream axes, resulting in a narrower scour footprint. Although CW scour typically shows no significant backfilling, a small depositional zone appears in the downstream wake. This minor deposition results from localized sediment resettlement from the eroded scour hole and not from ongoing upstream sediment supply.

The LB condition produces a shallower scour hole with rougher, more irregular contours but narrower lateral extent around the pier compared to the CW condition. The maximum depth is 0.076 m (z/D = 1.52), approximately 11.8% lower than the CW value, demonstrating that continuous, upstream sediment supply from upstream helps limit scour development. Ongoing sediment transport, maintained by the recirculating system, causes simultaneous erosion near the pier and partial backfilling in the downstream wake. This backfilling creates low sediment mounds that partly fill the scour hole, disrupting the smooth bedform seen in the CW condition. The greater longitudinal extension indicates a redistribution of erosive action along the flow direction, likely due to changes in the near-bed flow structure caused by incoming sediment. These changes alter both the upstream flow patterns and the wake vortex downstream, resulting in a more elongated but shallower scour footprint.

These morphological distinctions are clearly illustrated in Figures 10 and 11 and are further supported by the longitudinal scour profiles at multiple azimuthal angles, (see Figure 12 in Section 4.3). The observed differences in scour depth and morphology between CW and LB conditions are consistent with previous findings reported by Melville & Coleman [19], who emphasized the role of sediment supply in limiting scour progression under LB conditions. Similarly, Farooq & Ghumman [25] demonstrated that different pier geometries under CW conditions produce varying scour patterns and depths. In contrast to their CW findings, the present study reveals that LB conditions with continuous sediment supply yield significantly shallower and more stable scour profiles, underscoring the mitigating effect of upstream sediment availability in controlling local scour intensity compared to sediment-starved CW environments

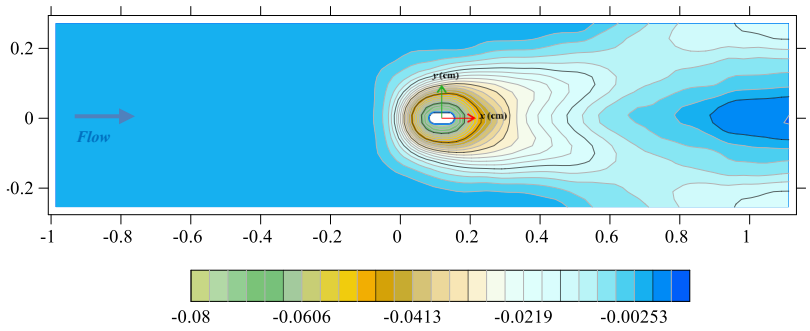

Figure 10. Bed elevation contour around an oblong pier under clear-water scour conditions

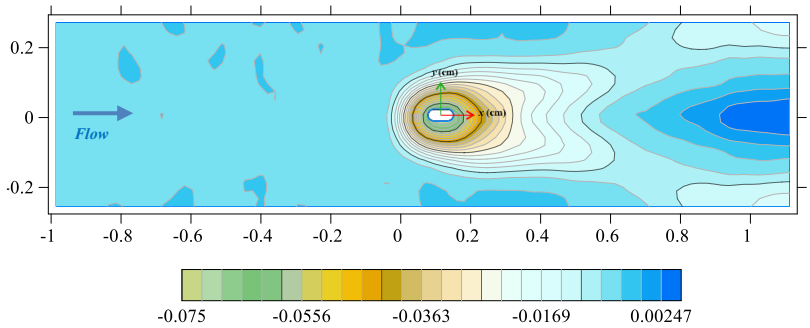

Figure 11. Bed elevation contour around an oblong pier under live-bed scour conditions

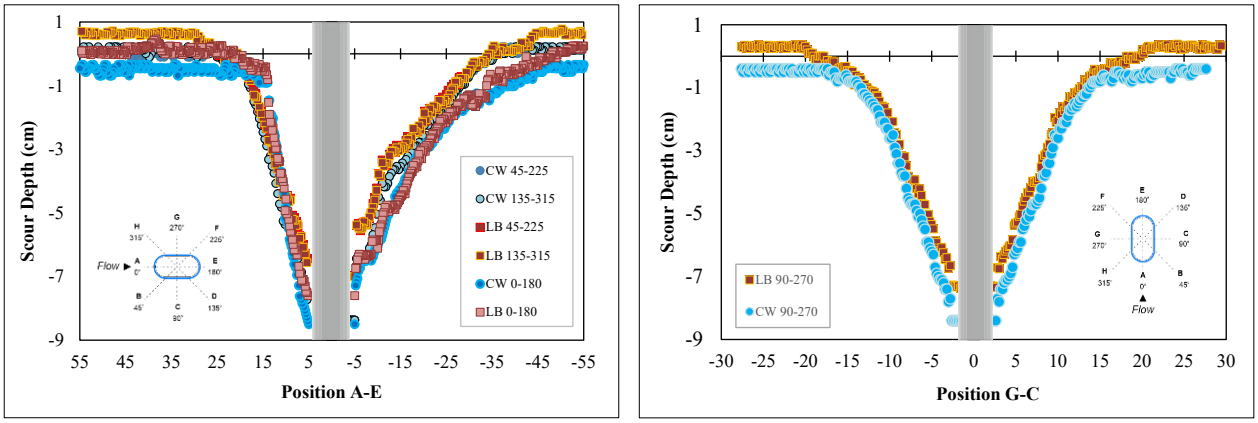

Figure 12. Longitudinal scour profiles at multiple azimuthal angles around the pier

Furthermore, the recorded maximum scour depths 0.085 m (z/D = 1.7) under CW and 0.076 m (z/D = 1.52) under LB conditions fall within the range reported by Sheppard et al. [18] for comparable pier Reynolds numbers and flow intensities. This agreement not only reinforces the validity of the present experimental setup but also confirms the governing influence of sediment-transport regimes on scour development mechanisms.

The observed scour morphological characteristics around oblong piers demonstrate strong consistency with previous comparative studies examining streamlined pier geometries. Chavan et al. [7] reported that oblong piers produce 15% shallower scour depths compared to circular piers under similar hydraulic conditions, which aligns with the streamlined geometry advantages observed in the present study. Their findings further confirm that oblong piers create smaller scour regions compared to bluff-body configurations, supporting the present observation that streamlined shapes effectively reduce scour intensity. Notably, Chavan et al. [7] documented that scour width increases significantly under seepage

conditions (28–44% for oblong piers), indicating that sediment-transport mechanisms redistribute erosive forces laterally around the pier. Although the present study shows CW conditions produce larger scour volumes (14.1% greater) and wider areas (28.1% larger) compared to LB conditions, both studies demonstrate that pier geometry significantly influences scour pattern development, with streamlined oblong shapes consistently providing superior scour resistance compared to circular configurations across different sediment-transport regimes.

4.3. Scour Morphology and Azimuthal Distribution

The bed morphology was analyzed to quantitatively identify the spatial characteristics of scour holes and sediment deposition patterns around the oblong pier due to complex flow interactions. The morphological data not only capture the geometric shapes of the scour features but also reflect the dynamic bed deformations that occurred throughout scour development. These findings support the interpretations previously derived from the temporal analysis, providing a more comprehensive understanding of the physical mechanisms behind bedform development. A summary of the key morphological and volumetric parameters describing the scour features is presented in Table 3.

Table 3. Scour geometry quantification parameters

Parameter	CW	LB	Difference
Angles (α)^{O}	40.50	37.70	CW > 7.4%
Scour Area (m^2)	0.491	0.424	CW > 15.6%
Ratio (l/D)	0.188	0.172	CW > 9.3%
Ratio (w/D)	0.082	0.064	CW > 28.1
Ratio (z/D)	1.7	1.5	CW > 11.8%
Scour volume (m^3)	0.0097	0.0085	CW > 14.1%

Note: α: the angle of maximum scour orientation relative to the flow direction; l/D: the ratio of scour length (parallel to flow) to pier diameter; w/D is the ratio of scour width (perpendicular to flow) to pier diameter; z/D: the ratio of maximum scour depth to pier diameter.

The experimental data show clear scaling relationships between scour dimensions. Scour volume increases non-linearly with depth in both transport regimes, with CW conditions showing a steeper scaling due to concentrated erosion. Area expansion follows similar nonlinear patterns, confirming that shallow scour underestimates total foundation exposure. The length-to-width aspect ratio remains consistent across experiments, indicating that pier geometry mainly controls the proportions of scour holes, while the transport regime affects their size. Under CW conditions, higher volume-to-area ratios suggest more efficient, concentrated erosion processes compared to the dispersed erosion patterns observed in LB conditions.

The scour geometry data show clear differences in shape between CW and LB scour patterns. Under CW conditions, the scour hole is much larger in volume (0.0097 m^3 compared to 0.0085 m^3, about 14.1% more) and wider laterally (w/D = 0.082 versus 0.064), indicating more focused and intense erosion around the pier. This shape forms because there is no incoming sediment, allowing continuous downward erosion until the local sediment-transport limit is reached. In contrast, the LB scour profile shows l/D = 0.172 versus CW with l/D = 0.188, indicating CW has a 9.3% higher length-to-diameter ratio. Although its length is greater, the total scour volume under LB conditions remains much lower because mobile sediments fill in during the experiment. These findings support the idea that sediment transport regimes influence not only the rate of scour but also the shape of the resulting bed.

Figure 12 displays the longitudinal scour depth profiles measured at various azimuthal angles around the oblong pier under both CW and LB conditions. The plot illustrates how scour depth changes along the flow and diagonal sections (0°–180°, 45°–225°, and 135°–315°), emphasizing the spatial patterns of erosion and deposition related to the pier's shape. The profiles in Figure 12 exhibit clear asymmetrical patterns, with the deepest scour depths located along the flow axis (0–180° azimuth), reaching approximately −8.5 cm for CW and −7.6 cm for LB. These upstream scour zones result from localized flow acceleration and impact at on the pier's upstream face, which causes bed material removal in that area. Downstream, sediment tends to accumulate, although the vertical recovery usually does not exceed +1.0 cm above the initial bed level in most profiles.

Diagonal profiles along 45°–225° and 135°–315° show moderately symmetrical scour patterns on both sides of the pier, indicating lateral flow redistribution around the elongated shape. Under clear-water (CW) conditions, scour depths are consistently deeper than those under LB conditions in all directions, confirming that continuous erosion occurs when there is no upstream sediment supply. In contrast, LB profiles show smoother and shallower contours, probably due to partial backfilling from recirculating sediments. A gradual geometric transition is observed from upstream scour to downstream deposition in both flow regimes, indicating a near-equilibrium between erosional

and depositional processes around the pier body. These longitudinal profiles also highlight the influence of pier orientation and flow direction on scour development, especially along the 0°–180° axis, where direct flow impingement on the pier nose increases local scour. Meanwhile, the transverse profile (90°–270°) exhibits nearly symmetrical scour shapes. The CW conditions create deeper scour than the LB conditions, indicating a consistent lateral flow distribution around the streamlined pier.

Figure 13 shows the normalized longitudinal scour depth profiles (z/D) along the flow axis (azimuth 0–180°) for the current oblong pier under CW and LB conditions, compared with various pier shapes reported by Farooq & Ghumman [25]. This comparison highlights how pier shape affects local scour patterns under similar hydraulic conditions. These patterns are characterized by the maximum scour just upstream of the pier and sediment deposits forming both upstream and downstream. This asymmetry shows how flow-pier interactions change under different sediment-transport regimes.

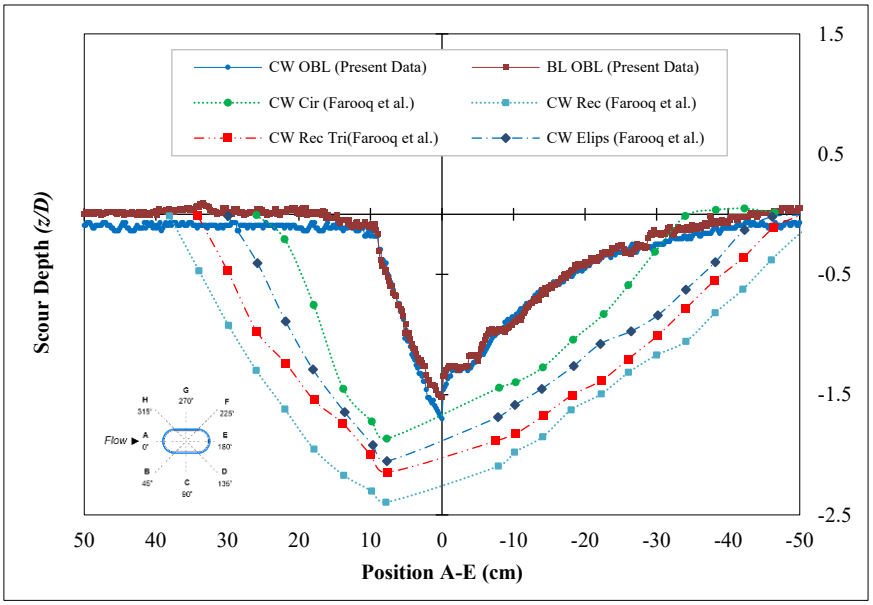

Figure 13. Longitudinal scour profiles for different pier shapes: The present oblong pier vs. literature data

Compared to data from Farooq & Ghumman [25], the present oblong pier displays the shallowest scour depths among all tested shapes, surpassing circular piers (which cause the deepest scour), as well as rectangular and triangular piers. The scour depth around the oblong pier is also like that of elliptical piers, further confirming the hydraulic efficiency of streamlined pier shapes. These findings demonstrate that oblong piers can significantly reduce local scour compared to bluff-body shapes, making them suitable for bridge foundations in sediment-laden flows [25]. This behavior aligns with well-known hydrodynamic processes that influence local scour: the flow at the upstream face of the pier initiates bed material removal, while the return flow and wake-vortex system downstream help carry the eroded sediment away from the pier base. The interactions between these upstream and downstream flow structures creates an asymmetrical longitudinal scour pattern, with more vertical erosion occurring upstream and gentler sediment redistribution downstream [13, 38]. Understanding these mechanisms is crucial for accurately predicting scour shapes and designing effective mitigation strategies.

4.4. Upstream and Downstream Velocity Distribution

To verify that the downstream sedimentation patterns observed in Figures 10 and 11 mainly result from sediment transport processes and horseshoe-vortex interactions, velocity distribution measurements were taken using an Acoustic Doppler Velocimeter (ADV). The measurements were performed on a reconstructed fixed-bed setup to eliminate bed mobility effects and ensure accurate flow-field analysis, thus preventing movable sediment particles from disrupting the ADV operation. Measurement points were carefully positioned at 1.5D upstream (0°) and 1.5D downstream (180°) from the pier centerline (Figure 14), corresponding to areas of maximum flow acceleration and wake formation, respectively, as indicated by the scour morphology analysis. These locations highlight key flow regions where the horseshoe-vortex system causes upstream erosion and where wake vortices facilitate downstream sediment transport and deposition. The velocity distribution within the 1.5D region is shown in Figure 14.

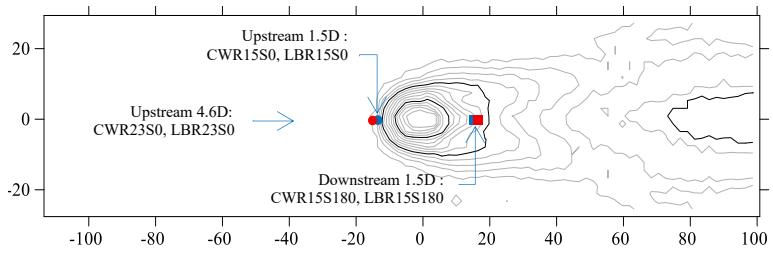

Figure 14. Velocity distribution measurement locations at 1.5D upstream and downstream

The velocity measurement data are organized using a systematic naming system that indicates the flow condition, measurement location, and angular position relative to the pier. The coding format is [Flow Condition][Distance from the pier][Angular Position], with each component providing specific details about the measurement parameters. The flow condition is represented by CW and LB, indicating the two distinct sediment-transport regimes examined in this study. The radial distance from the pier centerline is denoted by R15 and R23, corresponding to 15 cm (1.5*D*) and 23 cm (4.6*D*), respectively, where *D* equals the pier width of 5 cm. The R15 location was chosen based on scour morphology analysis to capture intense flow-structure interactions, serving as a strategic measurement point, while R23 was selected to establish reference log-law velocity profiles (Equation 3) under undisturbed flow conditions beyond the pier's immediate influence zone. The angular position uses S0 for 0° (upstream stagnation point) and S180 for 180° (downstream wake region), defining the azimuthal orientation relative to the flow direction. For example, CWR15S0 refers to clear-water flow measurements taken 15 cm from the pier at the upstream position (0°), while LBR23S0 indicates bed-load flow measurements taken 23 cm upstream in the undisturbed flow region. This nomenclature offers a clear and consistent framework for identifying and comparing velocity profiles across different flow conditions and measurement locations throughout the study.

To investigate the flow mechanisms governing scour morphology differences, comprehensive three-dimensional velocity measurements were conducted around the oblong pier under both CW and LB conditions. The velocity profiles presented in Figure 15 were obtained at locations of 1.5*D* (R15 = 15cm) and 4.6D (R23 = 23 cm) from the pier centerline, specifically at the upstream stagnation point (θ = 0°) and downstream wake region (θ = 180°). The inclusion of R23 measurements provides insight into flow recovery patterns beyond the immediate pier influence zone, while R15 data captures the intense flow-structure interactions responsible for scour development. As noted earlier, these measurements were performed on a reconstructed fixed-bed representing the equilibrium scour geometry to eliminate transient fluctuations, with theoretical log-law velocity profiles overlaid to validate turbulent boundary layer behavior and assess flow development characteristics.

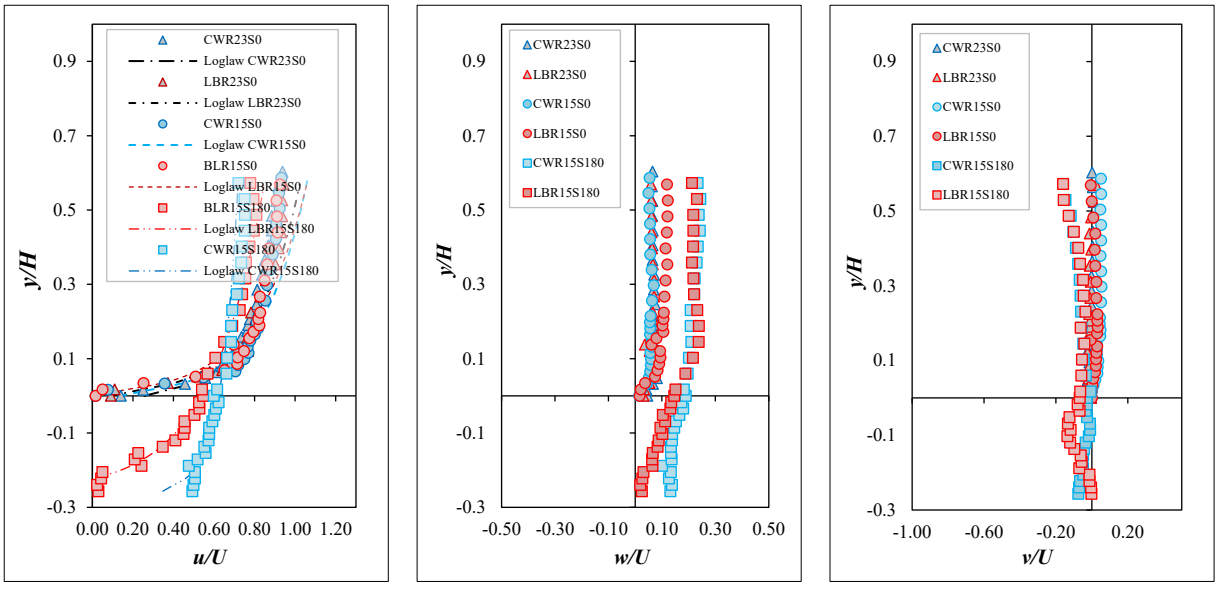

Figure 15. Velocity profiles (*u*/*U*, *w*/*U*, and *v*/*U*) at 1.5*D* from the pier centerline upstream and downstream

The streamwise velocity (*u*/*U*) reveals fundamental contrasts between CW and LB conditions. At the near-pier position R15S0, both regimes exhibit a distinct inner region ($y/H < 0.2$) with relatively coincident profiles that closely follow the log-law, indicating that near-bed turbulent structures remain largely unaffected by different sediment-transport regimes despite the pier's proximity. In the outer region ($y/H > 0.3$), CW and LB display relatively coincident velocity profiles that deviate slightly from the classical log-law as the flow recovers from pier influence, showing that the blockage effect, rather than sediment regime, governs outer-region behavior at this location.

Farther out at R23S0, a similar pattern is observed: CW ($u*$ = 0.054) and LB ($u*$ = 0.080) again exhibit relatively coincident outer-region profiles that still show minor departures from the log-law, while their inner-region profiles continue to fit the log-law well. Based on classical boundary-layer theory and supporting measurements at greater distances, the velocity profiles are expected to converge fully toward the canonical log-law as the influence of the pier diminishes. In the downstream wake (R15S180), both profiles remain broadly consistent with the log-law, although their outer-region gradients differ from the classical trend due to wake-induced flow adjustments. CW exhibits a pronounced reduction in friction velocity ($u*$ = 0.027), whereas LB maintains higher bed shear ($u*$ = 0.087), supporting the partial backfilling evident in scour morphology. All $u*$ values exceed the critical threshold ($u*_{(cr)}$ = 0.04), confirming that upstream sediment availability—continuous in LB and absent in CW—rather than flow intensity dictates the contrasting scour response.

Vertical velocity (w/U) measurements capture the dynamics of the horseshoe-vortex. At R15S0, strong downflow (≈ –0.3 U) drives sediment entrainment, with CW slightly more intense (–0.32 U) than LB (–0.28 U), a 12 % difference consistent with the 11.8 % greater scour depth under CW conditions. By R23S0, vertical motions decay to near zero, demonstrating that horseshoe-vortex influence extends only two to three pier diameters. At R15S180, upward motion (≈ +0.2 U) reflects wake-vortex development, with LB exhibiting larger fluctuations that explain its 16.1 % greater length-to-diameter scour ratio.

The lateral velocity (v/U) illustrates asymmetric flow redistribution. At R15, CW reaches ±0.3 U, producing a concentrated, symmetric scour hole, whereas LB shows weaker and more irregular motions (±0.2 U) that, together with continuous sediment supply, foster shallow, laterally diffuse erosion and a more elongated but shallower scour footprint. At R23, lateral components in both regimes diminish to near-background levels.

Collectively, these multilocation measurements confirm that intense three-dimensional turbulence within about two to three pier diameters governs scour formation. Clear-water conditions exhibit a much higher volume-to-area ratio (≈ 0.0198 vs ≈ 0.0201 for LB), fully consistent with Table 3, which lists V/A ≈ 0.0198 for CW and ≈ 0.0201 for LB. This high ratio indicates more efficient and concentrated erosion, producing 14.1% greater scour volume and deeper holes. In contrast, LB's continuous sediment input dampens turbulence and redistributes shear, yielding wider but shallower scour.

4.5. Comparative Model Validation with Literature

4.5.1. Empirical Model Prediction

To evaluate the predictive accuracy of commonly used empirical formulas, this study compared measured equilibrium scour depths with estimates from selected models. The hydraulic and geometric parameters used for calculations are summarized in Table 4. The predicted scour depths were expressed in non-dimensional form (z/D), where z is the maximum equilibrium scour depth and D is the pier width, allowing for standardized comparisons across different models and flow conditions. Three empirical formulas were selected for comparison: Melville [16], Richardson/HEC-18 [17], and Sheppard et al. [18]. Each formula incorporates different assumptions about pier geometry, sediment mobility, and hydraulic parameters. Although many empirical Equations exist for scour prediction, research specifically focusing on oblong-shaped piers is limited compared to studies on cylindrical or rectangular piers. The following provides a brief overview of each formula:

- Melville's Formula (1997) [16]:

$$z_{eq} = k_I k_h k_d k_{sh} k_{\alpha,\frac{L}{B}} \tag{3}$$

where, k_{sh} is the shape factor, k_a, L/B is the alignment and length to breadth ratio factor, D is the sediment diameter, u is the mean flow velocity, and g is the acceleration due to gravity. To evaluate the predictive accuracy of commonly used empirical formulas, this study compared measured equilibrium scour depths with theoretical estimates from selected models. This formula was developed as a comprehensive equation for various pier shapes including circular, rectangular (both round-nosed and square-nosed).

- Richardson/HEC-18 Formula (1975) [17]:

$$\frac{z_{eq}}{h} = 2.0 k_1 k_2 k_3 k_4 \left[\frac{D}{h}\right]^{0.65} \left(\frac{u}{\sqrt{gh}}\right)^{0.43} \tag{4}$$

where, k_{sh} is the shape factor, k_a, L/B is the alignment and length to breadth ratio factor, D is sediment diameter, u is the mean flow velocity, and g is the acceleration due to gravity. This formula was originally developed primarily for cylindrical piers but later extended to accommodate multiple pier shapes including circular, square, rectangular, and triangular piers.

- Sheppard's Formula (2004) [18]:

$$\frac{z_{eq}}{h} = 2{,}5 f_1\left(\frac{y_0}{D^*}\right) f_2\left(\frac{u}{u_c}\right) f_3\left(\frac{D^*}{d_{50}}\right) \quad (5)$$

where, f_1, f_2, and f_3 are dimensionless functions representing various influencing factors, y_0 is water depth, D^* is the shape factor, u is the mean velocity, u_c is the critical velocity, and d_{50} is the median grain size of the bed material. This formula was initially formulated based on experimental data from circular piers but designed with general hydrodynamic parameters that allow application to other pier geometries through parameter adjustments and modifications of empirical constants.

Table 4. Hydraulic and geometric parameters used in scour prediction

Parameter	Value
Flume length	10 m
Flume width (B)	0.6 m
Median grain size (d_{50})	2.21 mm
Water depth (h)	0.1 m
Discharge (Q)	50 L/s
Pier width (D)	0.05 m
Pier length (l)	0.10 m
Relative pier size (D/d_{50})	22.6 (-)
Ratio of flow depth and pier width (h/D)	2.0 (-)

It should be noted that none of these formulas were originally developed specifically for oblong piers. Melville's formula provides the most comprehensive treatment by explicitly including oblong shapes with dedicated shape factors, while Richardson's and Sheppard's formulas require parameter adaptations from their original circular/cylindrical pier foundations. The three empirical formulas were applied with appropriate parameter adjustments to account for different flow regimes. For Melville's formula, the sediment size factor (k_d) was modified based on bed mobility conditions. Richardson's formula employed different bed condition factors (k_3 = 1.1 for clear-water and k_3 = 1.0 for live-bed conditions). Sheppard's formula utilized flow intensity ratios (u/u_c) with $u/u_c \leq 1.0$ for clear-water conditions and $u/u_c > 1.0$ for live-bed conditions, reflecting different transport capacities.

The input parameters used in these formulas and their specific values in the current experiment are shown in Table 3. The key difference among these formulas, especially regarding pier shape and flow conditions, is how they treat the shape factor and sediment-transport considerations. For example, Melville uses a fixed k_{sh} = 0.75 for oblong piers, while Richardson employs k_1 = 0.8 along with a variable bed condition factor k_3, and Sheppard requires adjustments to constants when applied to non-cylindrical piers. These differences lead to a validation effort using experimental data specific to oblong geometries and y/D = 2.0. Other relevant parameters used are presented in Table 4.

Using the formulas above and parameters from Table 4, the predicted scour depths were calculated and compared to experimental results listed in Table 5. Under CW conditions, both Melville's and Sheppard's models predicted z/D = 1.84, while Richardson's model provided a higher estimate of z/D = 1.96. The actual measured scour depth in CW was z/D = 1.70, resulting in deviations of 8% and 15%, respectively. For LB, the measured z/D was 1.52, with predictions ranging from 1.56 (Sheppard, 3% deviation) to 1.80 (Richardson, 18% deviation). To provide a quantitative assessment of model performance beyond simple percentage deviations, statistical validation metrics were employed to evaluate prediction accuracy. Root Mean Square Error (RMSE) quantifies the magnitude of prediction errors in dimensionless units, with lower values indicating better model performance. Mean Absolute Percentage Error (MAPE) expresses prediction accuracy as a percentage, where values below 10% indicate excellent accuracy, values between 10% and -20% represent good accuracy, and above 20% suggest reasonable to poor performance. These complementary metrics provide both absolute and relative measures of model reliability for engineering applications. Based on Table 5, the superior statistical performance of Sheppard's model (MAPE = 5.4%) compared to Melville (10.0%) and Richardson (16.9%) validates its suitability for reliable oblong pier scour prediction in engineering practice.

Table 5. Theoretical and experimental equilibrium scour results

Parameter	Pier Shape	Prediction Scour $\frac{z_{eq}}{D}$	Experimental Scour $\frac{z_{eq}}{D}$	Deviation	RMSE	MAPE	Performance Bar
Melville CW	Oblong	1.84	1.70	8%	0.161	10.0%	
Melville LB	Oblong	1.70	1.52	12%			
Richardson CW	Cylindrical	1.96	1.70	15%	0.270	16.9%	
Richardson LB	Cylindrical	1.80	1.52	18%			
Sheppard CW	Cylindrical	1.84	1.70	8%	0.103	5.4%	
Sheppard LB	Cylindrical	1.56	1.52	3%			

Note: Performance bars visualize model accuracy based on MAPE values, with fuller bars indicating better predictive performance

Among the models evaluated, Sheppard's formula showed the smallest deviation from experimental values for both flow regimes, demonstrating its adaptability. Richardson's overprediction indicates that its parameters may not fully capture the effects of oblong geometry and mobile-bed dynamics. Although Sheppard's model was originally designed for cylindrical piers, its focus on general hydrodynamic parameters rather than shape-specific corrections allows for wider use. Additionally, the hydraulic conditions in this study, especially the subcritical flow, sediment mobility, and aspect ratio ($y/D = 2.0$), closely align with those under which Sheppard's equation was developed, boosting its predictive accuracy.

4.2.5. Comparison with Previous Studies

A broader comparison with prior literature supports the validity of the present results. As shown in Table 6, the experimental values obtained in this study ($z/D = 1.70$ for CW and 1.52 for LB) fall within the range reported by previous studies for oblong piers with similar y/D ratios. For example, Chavan et al [7], Bento et al [22], and Pahlevi et al [39] documented z/D values ranging from 1.2 to 1.85 under comparable conditions with y/D between 1.5 and 2.8.

Table 6. Comparison with previous research

Research	Pier Shape	*y/D*	*l/D*	*z/D*	Flow
Chavan et al. [7]	Oblong	1.8-2.5	2.0	1.4-1.8	CW
Chavan et al. [7]	Cylindrical	1.8-2.5	1.0	1.9-2.2	CW
Bento et al. [22]	Oblong	1.5-2.2	1.8	1.2-1.6	CW
Pahlevi et al. [39]	Oblong	2.0-2.8	2.0	1.3-1.7	CW
Pahlevi et al. [39]	Oblong	2.0-2.8	1.0	1.8-2.3	CW
Sheppard & Miller [38]	Cylindrical	2.0-4.0	1.0	1.8-2.3	CW
Present study	Oblong	2.0	2.0	1.70	CW
Present study	Oblong	2.0	2.0	1.52	LB

Note: CW = Clear-water scour, LB = Live-bed scour, scour depth (z/D), Ratio of pier width and length (l/D) and Ratio of flow depth and pier width (y/D)

Furthermore, it has been consistently observed that oblong piers cause 15%–25% shallower scour depths compared to cylindrical ones, as confirmed by Sheppard and Miller [38], Pahlevi et al [39], and Vijayasree et al [21]. This is due to the streamlined shape of oblong piers, which reduces the strength of upstream vortical flow structures and delays flow separation near the pier base. Additionally, the study highlights how sediment-transport conditions influence scour development. Under LB conditions, where upstream sediment is continuously supplied, the measured z/D was 1.52, reflecting an 11.8% reduction compared to the CW case (1.70). This level of reduction aligns well with previous studies on cylindrical piers, such as that of Sheppard et al. [18], who reported scour depth reductions of 8%–15% under similar transitions from CW to LB.

5. Conclusions

Based on the laboratory flume experiments and subsequent analyses, the key findings are summarized as follows:

- CW scour develops 36.4% faster (T^* = 666 min) and reaches 11.8% greater equilibrium depth (z/D = 1.70) compared to LB conditions (T^* = 909 min, z/D = 1.52), indicating a higher immediate risk requiring more frequent monitoring during floods.
- CW produces symmetric, steep-walled scour holes with 14.1% larger volume and 15.6% wider planform area, creating vertical undermining risk through concentrated deep erosion. LB generates shallower but more elongated scour with pronounced downstream backfilling, leading to gradual longitudinal foundation undermining rather than sudden collapse.

- Velocity measurements confirm that stronger vertical downflow (w/U = -0.32) drives aggressive entrainment in CW conditions, while enhanced lateral fluctuations under LB conditions explain the observed, more elongated, irregular scour patterns. The 12% reduction in downflow intensity correlates directly with the 11.8% scour depth reduction.
- The 15%–25% scour reduction for oblong versus cylindrical piers confirms streamlined geometry advantages. However, the wider lateral spread under LB conditions necessitates adequate lateral scour protection despite shallower depths, highlighting the importance of considering both sediment-transport regimes in tropical river environments.
- Sheppard's formula demonstrates superior performance (MAPE = 5.4%) compared to Melville's (10.0%) and Richardson's (16.9%) models, with deviations of only 8% (CW) and 3% (LB) from the experimental values, validating its applicability for oblong pier scour prediction despite being originally developed for cylindrical piers.

These findings emphasize that although streamlined pier designs enhance scour resistance, effective countermeasure strategies must account for regime-specific morphological characteristics to ensure long-term structural safety in sediment-laden rivers.

6. Declarations

6.1. Author Contributions

Conceptualization, B.A.K. and A.R.D.; methodology, A.R.D.; software, I.I. and A.R.D.; validation, B.A.K. and I.I.; formal analysis, A.R.D.; investigation, A.R.D. and B.A.K.; resources, I.I.; data curation, B.A.K.; writing—original draft preparation, A.R.D. and B.A.K.; writing—review and editing, A.R.D., B.A.K., and I.I.; visualization, I.I.; supervision, B.A.K.; project administration, B.A.K. and A.R.D.; funding acquisition, B.A.K. All authors have read and agreed to the published version of the manuscript.

6.2. Data Availability Statement

The data presented in this study are available in the article.

6.3. Funding and Acknowledgments

The authors would like to express their sincere gratitude and appreciation to the Indonesian Education Scholarship (BPI), the Center for Higher Education Funding and Assessment (PPAPT), the Ministry of Higher Education, Science, and Technology of the Republic of Indonesia, and the Indonesia Endowment Fund for Education (LPDP) for supporting this research through the Doctoral Scholarship Scheme. The authors also gratefully acknowledge the Department of Civil and Environmental Engineering, Faculty of Engineering, Universitas Gadjah Mada, Indonesia, for providing laboratory facilities, technical assistance, and support related to the preparation and submission of this manuscript.

6.4. Conflicts of Interest

The authors declare no conflict of interest.

7. References

[1] Wardhana, K., & Hadipriono, F. C. (2003). Analysis of Recent Bridge Failures in the United States. Journal of Performance of Constructed Facilities, 17(3), 144–150. doi:10.1061/(asce)0887-3828(2003)17:3(144).

[2] Vaza, H. (2016). Research on the improvement of Bridge Management System 1992 'Case of Bridge Condition Assessment in the Decentralized Indonesia'. PhD Thesis, University of Tsukuba, Tsukuba, Japan.

[3] Vaza, H., Irawan, R.R., Sukmara, G., Chairulloh, A.R. (2017). Determining the condition value and comfort level of bridges (1st Ed.). Vol. 3, Pusat Litbang Jalan dan Jembatan, Jakarta, Indonesia. (In Indonesian).

[4] Graf, W. H., & Yulistiyanto, B. (1998). Experiments on flow around a cylinder; The velocity and vorticity fields. Journal of Hydraulic Research, 36(4), 637–654. doi:10.1080/00221689809498613.

[5] Babaeyan-Koopaei, K. (2003). Flow pattern in the scour hole around a cylinder. Journal of Hydraulic Research, 41(4), 443–446. doi:10.1080/00221680309499989.

[6] Chen, W.-F., & Duan, L. (Eds.). (2013). Handbook of International Bridge Engineering. CRC Press, Boca Raton, United States. doi:10.1201/b15520.

[7] Chavan, R., Venkataramana, B., Acharya, P., & Kumar, B. (2018). Comparison of Scour and Flow Characteristics Around Circular and Oblong Bridge Piers in Seepage Affected Alluvial Channels. Journal of Marine Science and Application, 17(2), 254–264. doi:10.1007/s11804-018-0016-6.

[8] Ettema, R., Kirkil, G., & Muste, M. (2006). Similitude of Large-Scale Turbulence in Experiments on Local Scour at Cylinders. Journal of Hydraulic Engineering, 132(1), 33–40. doi:10.1061/(asce)0733-9429(2006)132:1(33).

[9] Fan, G., Li, H., Wang, T., Che, J., Li, X., Dou, C., & Wu, T. (2025). Study on scour simulation and boundary condition conversion technology for a shallow foundation bridge. Scientific Reports, 15(1), 1. doi:10.1038/s41598-025-86549-z.

[10] Baranwal, A., & Das, B. S. (2024). Scouring around bridge pier: A comprehensive analysis of scour depth predictive equations for clear-water and live-bed scouring conditions. Aqua Water Infrastructure, Ecosystems and Society, 73(3), 424–452. doi:10.2166/aqua.2024.235.

[11] Ahmed, F., & Rajaratnam, N. (1998). Flow around Bridge Piers. Journal of Hydraulic Engineering, 124(3), 288–300. doi:10.1061/(asce)0733-9429(1998)124:3(288).

[12] Chiew, Y. M., & Melville, B. W. (1987). Local scour around bridge piers. Journal of Hydraulic Research, 25(1), 15–26. doi:10.1080/00221688709499285.

[13] Kirkil, G., Constantinescu, S. G., & Ettema, R. (2008). Coherent Structures in the Flow Field around a Circular Cylinder with Scour Hole. Journal of Hydraulic Engineering, 134(5), 572–587. doi:10.1061/(asce)0733-9429(2008)134:5(572).

[14] Reddy, S. K., Kalathil, S. T., & Chandra, V. (2024). Local Scour around Different-Shaped Bridge Piers. Civil Engineering Journal, 10(6), 2019–2039. doi:10.28991/cej-2024-010-06-019.

[15] Melville, B. W., & Chiew, Y.-M. (1999). Time Scale for Local Scour at Bridge Piers. Journal of Hydraulic Engineering, 125(1), 59–65. doi:10.1061/(asce)0733-9429(1999)125:1(59).

[16] Melville, B. W. (1997). Pier and Abutment Scour: Integrated Approach. Journal of Hydraulic Engineering, 123(2), 125–136. doi:10.1061/(asce)0733-9429(1997)123:2(125).

[17] Arneson, L. A. (2013). Evaluating scour at bridges. FHWA-HIF-12-003, Federal Highway Administration, Washington, United States.

[18] Sheppard, D. M., Odeh, M., & Glasser, T. (2004). Large Scale Clear-Water Local Pier Scour Experiments. Journal of Hydraulic Engineering, 130(10), 957–963. doi:10.1061/(asce)0733-9429(2004)130:10(957).

[19] Melville, B. W., & Coleman, S. E. (2000). Bridge scour. Water Resources Publication, Colorado, United States.

[20] Kumar, V., Raju, K. G. R., & Vittal, N. (1999). Reduction of Local Scour around Bridge Piers Using Slots and Collars. Journal of Hydraulic Engineering, 125(12), 1302–1305. doi:10.1061/(asce)0733-9429(1999)125:12(1302).

[21] Vijayasree, B. A., Eldho, T. I., Mazumder, B. S., & Ahmad, N. (2019). Influence of bridge pier shape on flow field and scour geometry. International Journal of River Basin Management, 17(1), 109–129. doi:10.1080/15715124.2017.1394315.

[22] Bento, A. M., Viseu, T., Pêgo, J. P., & Couto, L. (2021). Experimental characterization of the flow field around oblong bridge piers. Fluids, 6(11), 1. doi:10.3390/fluids6110370.

[23] Baduna Koçyiğit, M., & Koçyiğit, Ö. (2024). Experimental Investigation of Bridge Scour under Pressure Flow Conditions. Water (Switzerland), 16(19). doi:10.3390/w16192773.

[24] Omara, H., Ookawara, S., Nassar, K. A., Masria, A., & Tawfik, A. (2022). Assessing local scour at rectangular bridge piers. Ocean Engineering, 266(P3), 112912. doi:10.1016/j.oceaneng.2022.112912.

[25] Farooq, R., & Ghumman, A. R. (2019). Impact assessment of pier shape and modifications on scouring around bridge pier. Water (Switzerland), 11(9), 14. doi:10.3390/w11091761.

[26] Dong, H., Li, Z., & Sun, Z. (2025). Study on the Mechanism of Local Scour Around Bridge Piers. Journal of Marine Science and Engineering, 13(6), 1. doi:10.3390/jmse13061021.

[27] Silvia, C. S. (2020). Effect Of Bridge Piers On Local Scouring At Alue Buloh Bridge Nagan Raya Regency. Journal of the Civil Engineering Forum, 1000, 37. doi:10.22146/jcef.57719.

[28] Oliveto, G., & Hager, W. H. (2002). Temporal Evolution of Clear-Water Pier and Abutment Scour. Journal of Hydraulic Engineering, 128(9), 811–820. doi:10.1061/(asce)0733-9429(2002)128:9(811).

[29] Graf, W. H. (1998). Fluvial hydraulics: Flow and transport processes in channels of simple geometry. John Wiley & Sons, Hoboken, United States.

[30] Folk, R. L., & Ward, W. C. (1957). Brazos River bar [Texas]; a study in the significance of grain size parameters. Journal of Sedimentary Research, 27(1), 3–26. doi:10.1306/74d70646-2b21-11d7-8648000102c1865d.

[31] Buffington, J. M., & Montgomery, D. R. (1997). A systematic analysis of eight decades of incipient motion studies, with special reference to gravel-bedded rivers. Water Resources Research, 33(8), 1993–2029. doi:10.1029/96WR03190.

[32] Blott, S. J., & Pye, K. (2001). Gradistat: A grain size distribution and statistics package for the analysis of unconsolidated sediments. Earth Surface Processes and Landforms, 26(11), 1237–1248. doi:10.1002/esp.261.

[33] Maini, M., Kironoto, B. A., Rahardjo, A. P., & Istiarto. (2025). Alternative Method for Determining Manning's Roughness Coefficient Using Two-Point Velocity in Equilibrium and Nonequilibrium Sediment Transport. Civil Engineering Journal (Iran), 11(7), 2666–2685. doi:10.28991/CEJ-2025-011-07-02.

[34] Goring, D. G., & Nikora, V. I. (2002). Despiking Acoustic Doppler Velocimeter Data. Journal of Hydraulic Engineering, 128(1), 117–126. doi:10.1061/(asce)0733-9429(2002)128:1(117).

[35] Raudkivi, A. J., & Ettema, R. (1983). Clear-Water Scour at Cylindrical Piers. Journal of Hydraulic Engineering, 109(3), 338–350. doi:10.1061/(asce)0733-9429(1983)109:3(338).

[36] Harlan, D., Rasyid, I., Nugroho, J., Adityawan, M. B., & Natakusumah, D. K. (2024). Modelling of Flow and Scour Around the Piers With Different Geometric Shapes. International Journal of GEOMATE, 26(113), 115–122. doi:10.21660/2024.113.g13375.

[37] Shahhosseini, M., Yue, S., Xu, J., Zhang, M., & Yu, G. (2025). Scour depth at a pile with a collar at bed level in clear-water current. Ocean Engineering, 320(March 2024), 120319. doi:10.1016/j.oceaneng.2025.120319.

[38] Sheppard, D. M., & Miller, W. (2006). Live-Bed Local Pier Scour Experiments. Journal of Hydraulic Engineering, 132(7), 635–642. doi:10.1061/(asce)0733-9429(2006)132:7(635).

[39] Pahlevi, C. A., Setyandito, O., Istiarto, Sudiyono, K. A., Pierre, A. J., & Juliastuti. (2021). Oblong Bridge Pier Shape Influence toward Flow Velocity Characteristic and Scour Depth. IOP Conference Series: Earth and Environmental Science, 794(1), 012058. doi:10.1088/1755-1315/794/1/012058.

[40] Breusers, H. N. C. (1965). Conformity and time scale in two-dimensional local scour. Waterloopkundig Laboratorium, Delft, Netherlands.

[41] Cardoso, A. H., & Bettess, R. (1999). Effects of Time and Channel Geometry on Scour at Bridge Abutments. Journal of Hydraulic Engineering, 125(4), 388–399. doi:10.1061/(asce)0733-9429(1999)125:4(388).

[42] Ahmad, N., Suif, Z., & Jelani, J. (2024). Temporal Development of Scour Around Wide Piers. International Journal of GEOMATE, 27(122), 132–139. doi:10.21660/2024.122.g13427.